ROYAL SOCIETY
OF CHEMISTRY

COMMUNICATION

Check for updates

Ultrahigh-efficiency desalination *via* a thermally-localized multistage solar still†

Zhenyuan Xu, [iD] ‡[ab] Lenan Zhang, [iD] ‡[b] Lin Zhao, [iD] ‡[b] Bangjun Li,‡[a] Bikram Bhatia,[b] Chenxi Wang,[a] Kyle L. Wilke,[b] Youngsup Song, [iD] [b] Omar Labban,[b] John H. Lienhard, [iD] [b] Ruzhu Wang [iD] *[a] and Evelyn N. Wang [iD] *[b]

Passive vapor generation systems with interfacial solar heat localization enable high-efficiency low-cost desalination. In particular, recent progress combining interfacial solar heating and vaporization enthalpy recycling through a capillary-fed multistage architecture, known as the thermally-localized multistage solar still (TMSS), significantly improves the performance of passive solar desalination. Yet, state-of-the-art experimental demonstrations of solar-to-vapor conversion efficiency are still limited since the dominant factors and the general design principle for TMSS were not well-understood. In this work, we show optimizing the overall heat and mass transport in a multistage configuration plays a key role for further improving the performance. This understanding also increases the flexibility of material choices for the TMSS design. Using a low-cost and free-of-salt accumulation TMSS architecture, we experimentally demonstrated a record-high solar-to-vapor conversion efficiency of 385% with a production rate of 5.78 L m^{-2} h^{-1} under one-sun illumination, where more than 75% of the total production was collected through condensation. This work not only significantly improves the performance of existing passive solar desalination technologies for portable and affordable drinking water, but also provides a comprehensive physical understanding and optimization principle for TMSS systems.

Water scarcity has become an increasingly severe global challenge as more than one-third of the world's population is affected by water shortage.[1,2] Seawater desalination is regarded as one of the most effective solutions to address water scarcity.[3] In the last decade, commercial large-scale desalination facilities including the newly built reverse osmosis plants and legacy installations with multi-stage flash evaporation and multi-effect distillation have partly relieved the water-shortage stress.[4,5] However, these technologies require well-developed infrastructure and centralized installations,

Broader context

Seawater desalination is a promising technology to address global scarcity of clean drinking water. Although several commercial approaches such as multistage flash and reverse osmosis exist at large-scales, they are not suited for developing regions due to the requirement of well-established infrastructure, centralized installation and significant energy consumption. Previous works using interfacial solar vapor generation in a portable floating structure enable passive desalination or distillation in various off-grid areas. However, the solar-to-vapor conversion efficiency, defined as the ratio of total vaporization enthalpy to total solar energy input, for most previous studies has been limited to below 100% as the vaporization enthalpy is lost to the ambient environment. Recent progress combining interfacial solar heating with vaporization enthalpy recycling experimentally demonstrated a significant improvement in solar desalination performance. However, the overall demonstrated performance is still limited compared to what is theoretically achievable. In this work, we demonstrate a thermally-localized multistage solar still for desalination that enables ultra-high efficiency *via* a detailed investigation of the heat and mass transport mechanisms. We show the potential of our approach using a scalable, low-cost, ten-stage device which achieved a solar-to-vapor conversion efficiency of 385% and total production rate of 5.78 L m^{-2} h^{-1} under one-sun illumination. The prototype device also addresses practical issues related to device operability including water collection and salt-rejection. Our experiments show that more than 75% of the vaporized water was collected through condensation. The salt-rejection capability was demonstrated by operating the device continuously during the daytime and allowing the accumulated salt to be passively rejected through diffusion during the night time. The design principles and device architecture demonstrated in this work could enable high-efficiency passive desalination technologies as well as other solar thermal applications.

which are not available in many developing regions.[6] Passive solar desalination systems with simple configuration and off-grid operation are attractive for several developing regions with abundant solar energy and seawater,[7–9] but the high cost of water production and large area requirements from low conversion efficiency (~35% from solar energy to water) have limited their adoption thus far.[8,10,11]

Recent developments in small-scale, affordable, passive and high-efficiency solar vapor generation for seawater desalination have leveraged interfacial solar heat localization and material

[a] *Institute of Refrigeration and Cryogenics, Shanghai Jiao Tong University, Shanghai 200240, China. E-mail: rzwang@sjtu.edu.cn*

[b] *Department of Mechanical Engineering, Massachusetts Institute of Technology, Cambridge, MA 02139, USA. E-mail: enwang@mit.edu*

† Electronic supplementary information (ESI) available. See DOI: 10.1039/c9ee04122b

‡ Equal contribution to this work

innovations to improve energy conversion efficiency.[12–27] However, the solar-to-vapor conversion efficiency is below 100%, if the vaporization enthalpy is lost to the surrounding environment.[8,27,28] Thus, harvesting and reusing the vaporization enthalpy is the key to enhance energy conversion efficiency.[29] Although this concept has already been widely deployed in the large-scale multiple-effect distillation plants[4] and some conventional solar stills,[30] realizing effective enthalpy recycling in small-scale systems with solar heat localization poses significant technological challenges. Few recent studies have demonstrated portable systems with solar heat localization which recycled vaporization enthalpy to generate electricity (with 1.23% electricity conversion efficiency[25]), drive extra evaporation (with 72%[31] and 138%[32] total solar-to-vapor conversion efficiencies), or produce fresh water and electricity simultaneously (with >110% solar-to-vapor conversion efficiency and 11% electricity conversion efficiency[33]). However, the demonstrated solar-to-vapor conversion efficiency – slightly above 100% – is still limited in comparison to what is theoretically achievable.

While most of the recent experimental demonstrations mainly focused on combining the benefits of multiple stages and heat localization to achieve a higher performance for solar desalination, the fundamental limits to the overall performance and the corresponding design strategies were not explored.[29] Therefore, opportunities to further develop a low-cost and high-performance architecture were not demonstrated. To tackle this challenge, we performed analysis to obtain a fundamental understanding of heat and mass transport within the device, which leads to an optimized design approaching the theoretical limit. We also fabricated a ten-stage salt-accumulation-free TMSS prototype using low-cost materials and demonstrated a

record-high solar-to-vapor conversion efficiency of 385% with production rate of 5.78 L m^{-2} h^{-1} under one-sun illumination.

Fig. 1 shows the basic concept of the TMSS. The first stage facing the incident sunlight consists of a layer of optically-transparent silica aerogel thermal insulation, a solar absorber, a capillary wick and a condenser which are aligned along the direction of solar illumination (Fig. 1a). Each of the subsequent stages is composed of a capillary wick and a condenser separated by an air gap (Fig. 1b). The condenser of the last stage is inserted into the bulk brine to maintain its temperature close to the ambient environment, which ensures a large vapor pressure gradient across each stage. The solar absorber, sandwiched between the silica aerogel layer and the first capillary wick, converts solar energy into heat. The silica aerogel suppresses heat losses from the solar absorber through conduction, convection, and radiation, due to its ultralow thermal conductivity and high infrared opacity.[34–36] Thermal energy is transferred from the absorber to the capillary wick attached on the backside, where brine is driven up by capillarity and evaporates due to the elevated temperature. Vapor travels across the air gap between the evaporator and condenser, releasing thermal energy through condensation. The condensed clean water at each stage is collected, while the released thermal energy is transferred to drive evaporation in the next stage (Fig. 1a and b), realizing enthalpy recycling.

The TMSS architecture enables high-performance desalination due to three key attributes that optimize heat and mass transport. First, vaporization enthalpy recycling is realized by the multistage configuration, where the latent heat released from the previous stage is harnessed by the next stage to induce evaporation.
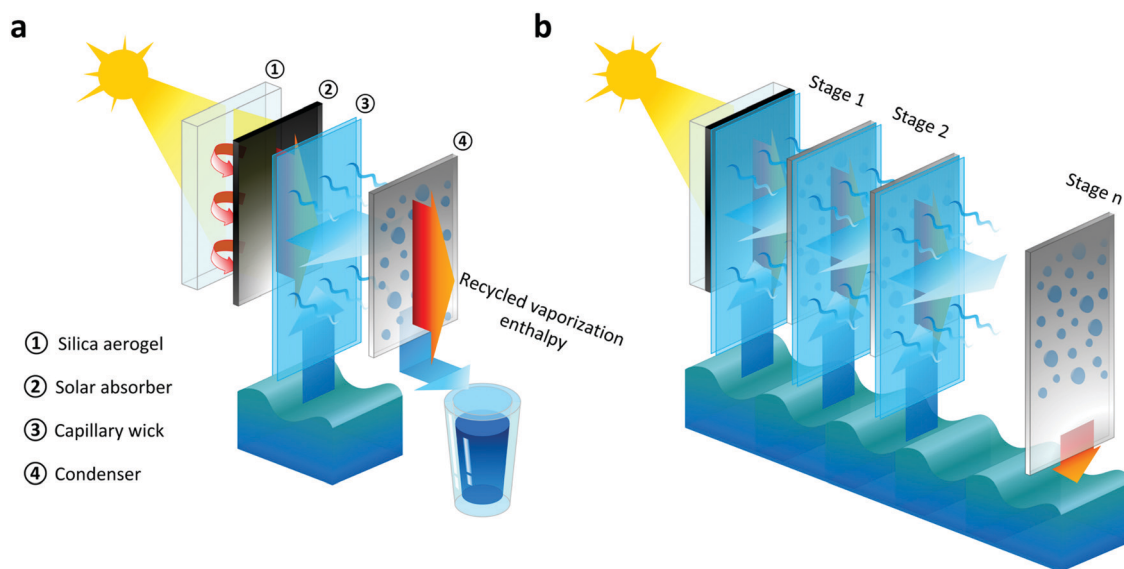

Fig. 1 Conceptual schematic of the TMSS device architecture. (a) Key components in the first stage of TMSS. The first stage consists of a solar-transparent monolithic silica aerogel thermal insulator, a solar absorber, a capillary wick, and a condenser. Solar energy is converted into heat and transferred from the absorber to the thin capillary wick. Evaporation occurs on the capillary wick due to interfacial heating. Brine is pumped from the reservoir due to capillary pressure to compensate for the loss of liquid in the capillary wick. The generated vapor travels across the air gap and condenses at the condenser. (b) Vaporization enthalpy recycling enabled by the TMSS architecture. Thermal energy released from condensation is transferred to the capillary wick, attached to the condenser of the previous stage, which drives evaporation in the next stage. The condenser of the last stage is inserted into the bulk brine to maintain a temperature close to ambient.

Secondly, unlike conventional interfacial solar heat localization approaches whose performance relies on thermally-insulating wicking materials that allow solar absorption and water evaporation at the same interface, the TMSS architecture decouples these functionalities where the solar absorption occurs on the front side while the interfacial heating and resultant evaporation are on the other side. This design provides more flexibility and permits the use of low-cost materials since it is possible to use any commercially available solar absorber having no wicking ability and any affordable capillary wick regardless of their solar absorptance. Finally, the vertically aligned layers with tunable tilt angles can significantly reduce the parasitic heat loss due to the negligible area of contact between the thin film evaporator and bulk brine (Fig. 1a), and enable operation for different sun positions due to geographical and seasonal variations.

To achieve the best performance, many design parameters including the width of the device a, air gap thickness b of each unit stage and the total number of stages n should be optimized (Fig. S1, ESI†). We chose a unit stage height of 10 cm since it is approximately equal to the wicking length of the capillary wick.[37] The choice of b and n was determined by considering the heat and mass transport in each stage. Specifically, reducing b can decrease the vapor transport resistance but increase the conduction loss through the gap. Although this conduction loss at a given stage can be reused by the next stage to promote evaporation, it reduces vapor generation at the previous higher-temperature stage leading to a decrease in the overall solar-to-vapor conversion efficiency. On the other hand, while increasing n always improves the overall performance in theory, in practice however, the benefit of adding more stages diminishes once the number of total stages is sufficiently large due to the inevitable heat loss from the sidewall. For this reason, the number of stages should also be optimized to ensure high solar-to-vapor conversion efficiency while avoiding additional cost of excessive stages. To determine the optimal configuration of the TMSS, we developed a theoretical model which describes these coupled effects of heat and mass transport (Fig. S1, ESI†).[38] Our theoretical analysis shows that an optimized air gap thickness exists for a given device height. For a = 10 cm, used in this study, the optimized $b \approx 2.5$ mm, corresponding to a peak solar-to-vapor conversion efficiency $\eta \approx 650\%$ (Fig. S2a and b, ESI†). In this configuration (i.e., a = 10 cm and b = 2.5 mm), the improvement of overall performance with the increase of the number of stages becomes insignificant when $n > 20$ (e.g., when n = 20, η = 600%). Based on practical considerations, we chose b = 5 mm to ensure the gap is larger than the typical droplet size on the condenser so that the condensate does not touch the evaporator and can be collected. For the proof-of-concept demonstration, we chose n = 10 to keep the device small and portable. Since this configuration (with a = 10 cm, b = 5 mm and n = 10) is close to the global optimal point, the predicted solar-to-vapor conversion efficiency is as high as 417% (Fig. S2b, ESI†). In addition, the theoretical model showed that effective thermal insulation of the sidewall is crucial to improve the efficiency since the heat loss from the side cannot be reused by the

following stages (Fig. S2c, ESI†). For this reason, we added 1.27 cm thick sidewall thermal insulation (thermal conductivity ≈ 0.022 W m^{-1} K^{-1}) to the prototype and incorporated its effect in the theoretical calculation. The theoretical analysis also demonstrated that it is critical to develop device design guidelines based on a fundamental understanding of heat and mass transport. Imprecise choice of design parameters can result in sub-optimal performance – for example, the solar-to-vapor conversion efficiency of a ten-stage device will decrease from 417% to 300% when the air gap is shrunk to 100 μm due to increased conduction loss, while the efficiency will be less than 250% when the air gap is larger than 1.5 cm owing to greater vapor transport resistance (Fig. S2b, ESI†).

Fig. 2a shows the prototype TMSS fabricated based on the design optimization described earlier. This ten-stage device consists of eleven nylon frames (Nylon PA12) which were fabricated using 3D printing (Fig. S3, ESI†). A 10 × 10 cm^2 commercial spectrally selective solar absorber (B-SX/T-L/Z-Z-1.88, Linuo-Paradigma) was embedded at the back of the first frame where a piece of glass (10 × 10 cm^2 area and 1 mm thick) with anti-reflection (AR) coating covered the front to protect the solar absorber (Fig. 2a). A monolithic silica aerogel (about 9.5 × 9.5 cm^2 and 5 mm thick) was placed between the solar absorber and the glass cover and served as transparent thermal insulation (Fig. S4, S5, ESI†). The other ten frames were identical (Fig. 2b). The condenser of each stage was a 0.5 mm thick aluminum plate (10 × 10 cm^2) which was fit into the frame from the back (Fig. 2b and Fig. S4, ESI†). To accelerate the removal of condensed water and avoid flooding, the condenser was coated with ≈ 1 μm thick Teflon AF to enable dropwise condensation (Fig. 2b and Note S.3, ESI†).[39,40] The advancing and receding contact angles on the hydrophobic coating were 108.2° and 103.2°, respectively (Fig. 2c and d). The small contact angle hysteresis ($\approx 5°$) allowed the condensed droplets of millimeter scale to be easily removed by gravity. To collect the desalinated water efficiently, a slot with $\approx 5.7°$ tilt angle was fabricated at the bottom of the frame which was connected to an outlet at the end (Fig. S3, ESI†). The high transparency (>95%) of the AR-coated glass and silica aerogel, as well as the high absorptance ($\approx 93\%$) of the solar absorber in the solar spectrum were confirmed by the UV-Vis-NIR spectrophotometer measurements (Fig. 2e). Due to the material flexibility of our new architecture, we used low-cost paper towels (Create-a-Size Paper Towels, Kirkland Signature™) as the capillary wick (with 10 cm width and 15 cm length), which was attached on the back of each condenser (Fig. 2f). The loosely packed cellulose fibers created numerous micropores (≈ 10 to 100 μm in diameter, Fig. 2g and h) which generated capillary pressure and enabled fast water transport. The total estimated material cost of this prototype based on retailers was $\approx \$1.54$ including the AR-coated glass, silica aerogel, solar absorber, paper towel evaporators, aluminum condensers and nylon frames (Note S.5, ESI†). Since nylon frames account for more than 70% of the cost, it is possible to further reduce the cost by replacing the existing partially-hollow frame design with fully-hollow structures to save material or switching to other cheaper alternatives.
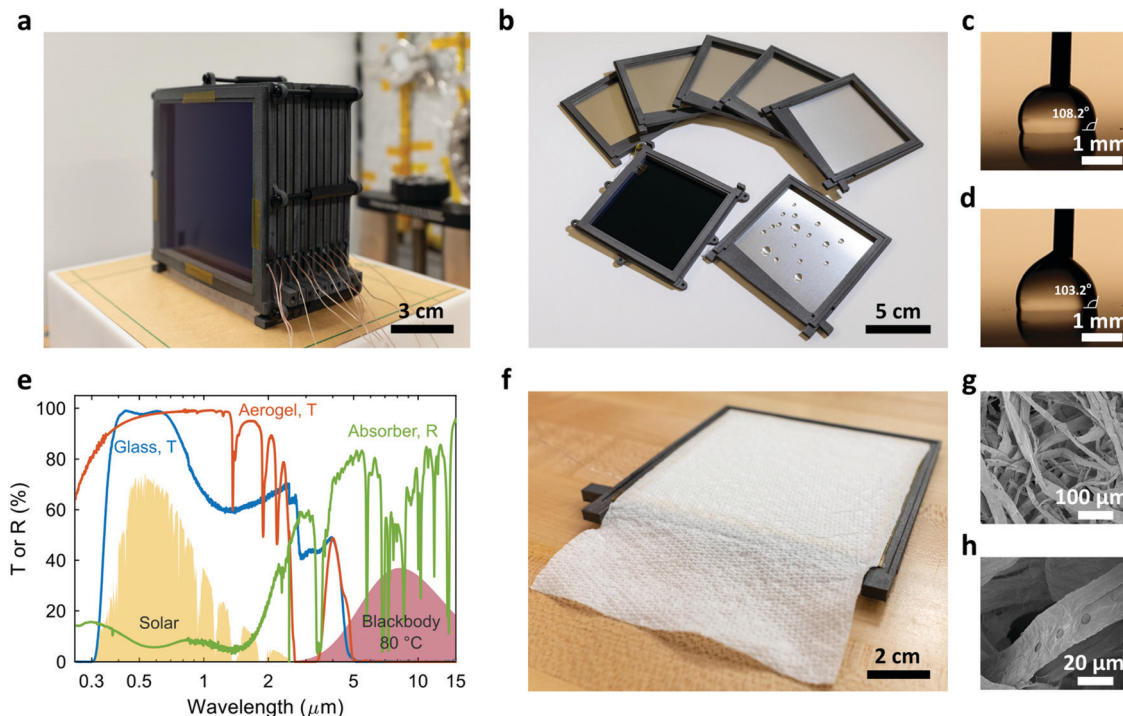
832 | Energy Environ. Sci., 2020, **13**, 830–839

This journal is © The Royal Society of Chemistry 2020

Fig. 2 Design and characterization of the ten-stage TMSS prototype. (a) Optical image of the device. The prototype was composed of eleven nylon frames, one solar absorber covered by a silica aerogel monolith, ten Teflon AF-coated aluminum condensers, and ten cellulose fiber (paper towel) evaporators. A piece of AR-coated glass was placed in front of the first stage to protect the silica aerogel and solar absorber. Eleven thermocouples were attached on the evaporator/condenser of each stage to monitor its temperature. One extra thermocouple was used to record the ambient temperature. (b) Optical image of the unit stages of the TMSS prototype. The nylon frame acted as a spacer to maintain the 5 mm thick air gap between the evaporator and condenser in each stage. A 0.5 mm thick aluminum plate with 1 µm thick Teflon AF hydrophobic coating was embedded into each frame as the condenser. Hydrophobic coating (c) advancing contact angle ($\approx 108.2°$), and (d) receding contact angle ($\approx 103.2°$) characterization. (e) Transmittance (T) and reflectance (R) spectra characterized by UV-Vis-NIR spectrophotometer. The AR-coated glass and silica aerogel transmitted nearly all of the incident solar radiation, while the low reflectance in the 0.3 to 1.5 µm wavelength range indicated high absorption of solar flux. The high reflectance of the solar absorber at longer wavelengths (>1.5 µm) reduced the thermal radiation loss. The solar spectrum and blackbody spectrum at 80 °C are plotted for reference. (f) Optical image of a representative evaporator attached on the back of a condenser. We used a low-cost paper towel as the evaporator which had high wickability due to its microporous structure. (g) and (h) show SEM images of the microporous structure of the evaporator. The loosely packed woven fibers created numerous pores with 10–100 µm in diameter.

The performance of the TMSS prototype was characterized in a laboratory environment (Note S.4, ESI†). Fig. 3a shows a schematic of the experimental setup. A solar simulator (92192, Newport Oriel Inc.) was used to provide uniform solar illumination (1000 W m^{-2}, one-sun). The TMSS device was supported by an acrylic box with an opening on the top for the capillary wicks to access the water reservoir. A balance (SJX6201N/E, Ohaus) was used to measure the mass loss of the reservoir continuously. An 1.27 cm thick thermal insulation (Super Tuff-R™, Dupont, thermal conductivity ≈ 0.022 W m^{-1} K^{-1}) was installed on the side wall to reduce the heat loss (Fig. S6, ESI†). To perform detailed thermal characterization, twelve thermocouples were used to measure the real-time temperature response where the first ten thermocouples monitored the evaporator/condenser temperature of each stage (labeled as T_1 to T_{10} respectively), while the remaining two thermocouples recorded the condenser temperature of the last stage (T_b) and the ambient temperature (T_{amb}), respectively (Fig. 2a and 3a). The temperature and mass loss data were collected by data acquisition equipment (34972A, Agilent) and processed by a computer. The transient temperature behavior of ten stages during a 3-hour operation is shown in

Fig. 3b. Because of the high thermal resistance of the silica aerogel and sidewall insulation, the temperature of the first stage rapidly increased to 60 °C (T_1) within 15 minutes and reached as high as 72 °C in steady state. The remaining stages were heated sequentially and gradually reached their steady states. After 100 minutes, all stages reached steady states. Although the condenser of the last stage was inserted into the water reservoir, its temperature still rose slightly above the ambient temperature ($T_b \approx 25$ °C) in steady state due to the thermal resistance through the thin aluminum sheet. Fig. 3c shows the change in weight of the reservoir during the test. The rate of mass change for the 10-stage device increased gradually and maintained at a constant value of ≈ 0.89 g min^{-1} after the thermal steady state was established. This dynamic behavior was precisely described by our time-dependent numerical model, also shown in Fig. 3c, which considers the temperature-dependent vapor concentration and diffusion at each stage (Note S.6, ESI†). The condensed water began to flow out from the outlet of the first stage approximately 8 minutes after turning on the solar flux, followed sequentially by the rest of the outlets (Video S1, ESI†). When the TMSS reached steady-state operation after 100 minutes,
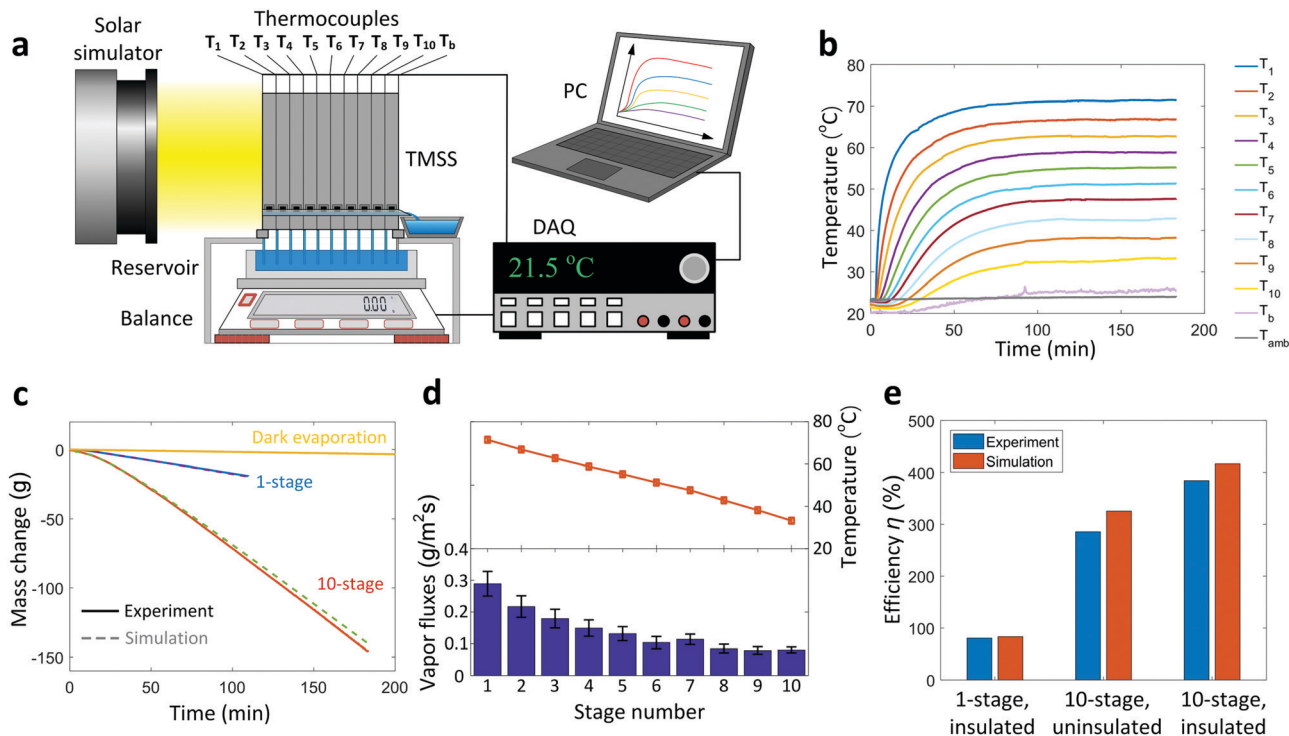
Fig. 3 Performance of the ten-stage TMSS device. (a) Schematic diagram of the experimental setup. A solar simulator provided the 1000 W m^{-2} solar flux. The real-time mass loss of the reservoir was measured using a balance and the temperature variations were characterized by twelve thermocouples – both recorded by a data acquisition equipment (DAQ) and processed by a computer (PC). (b) Temperature evolution of each stage during a 3-hour test. The temperature of the condenser in the last stage was maintained close to the ambient temperature throughout the test. It took the first stage ≈50 minutes and the entire TMSS device ≈100 minutes to reach thermal steady state. (c) Real-time mass loss of the ten-stage device and a one-stage device for comparison. The evaporation in dark conditions (labeled as Dark evaporation) is also shown for reference. Experimental results agree well with simulations which used the experimentally measured temperature as the input. (d) Temperature and corresponding vapor mass flux of each stage during steady state. The uncertainty in the temperature, measured using K-type thermocouples, was 1.5 °C. The vapor mass fluxes of each stage were evaluated using Fick's law of diffusion based on the temperature measurements and the corresponding uncertainties were propagated based on the temperature-dependent vapor concentration and diffusivity (Note S.6, ESI†). (e) Solar-to-vapor conversion efficiency of a thermally insulated ten-stage TMSS device compared with a one-stage and an uninsulated ten-stage device. The solar-to-vapor conversion efficiency of the ten-stage was approximately five times that of the one-stage device. Removing the sidewall thermal insulation led to a ≈100% (from 385% to 286%) reduction in the solar-to-vapor conversion efficiency for the ten-stage device. Experimental results show good agreement with numerical simulation.

continuous water flow was observed from all ten outlets (Video S2, ESI†). We measured ≈150 g total mass loss and collected 113 g condensed water from ten outlets after the 3-hour test, indicating ≈75% water collection. The discrepancy between the total mass of water lost and collected was due to the small droplets pinned on the condenser layers and leakage of vapor during operation. The collection efficiency can be further enhanced by increasing the condenser hydrophobicity and improving the sealing of each stage. Subtracting the contribution of evaporation in dark conditions (Fig. 3c) from the steady-state mass loss rate, the vapor production rate of our ten-stage TMSS under steady-state operation was 5.78 L m^{-2} h^{-1}.

The solar-to-vapor conversion efficiency η can be calculated from the production rate and is given by,

$$\eta = \frac{\dot{m} h_{\text{fg}}}{q_{\text{solar}}'' A} \quad (1)$$

where $\dot{m}$ is the vapor production rate under steady state, h_{fg} is the enthalpy of water vaporization, q_{solar}'' is the input solar flux (1000 W m^{-2}), and A is the effective solar absorbing area.

In this study, we used h_{fg} = 2394 kJ kg^{-1}, which corresponds to the latent heat at 45 °C, i.e., the average vapor temperature. To be conservative, we did not include the contribution of sensible heat to the solar-to-vapor conversion efficiency in our calculation. The effective absorbing area was $A = 9.6 \times 9.6$ cm^2 as defined by the aperture size of the frame. The demonstrated cumulative solar-to-vapor conversion efficiency of this ten-stage TMSS prototype was 385%, which agrees well with the theoretically predicted performance (417%). The corresponding gained output ratio (GOR), representing the number of times the latent heat has been reused,[29] is larger than four, indicating an efficient reuse of vaporization enthalpy based on the current design.

To further understand the heat and mass transport mechanism within the TMSS, we analyzed the temperature and vapor flux at each stage during the steady state (Fig. 3d). The temperature of each stage was averaged within the last hour of the measurement (i.e., from 120 to 180 minutes of the test). The temperature showed a nearly linear decay across the stages due to the similar thermal resistance of each stage. To elucidate the contribution of each stage to the total water production, we calculated the

834 | Energy Environ. Sci., 2020, 13, 830–839

This journal is © The Royal Society of Chemistry 2020

saturated vapor concentration based on the evaporator temperature and estimated the vapor flux using Fick's law of diffusion (Note S.6, ESI†). The uncertainty of vapor flux was evaluated by propagating uncertainties of mass diffusivity and vapor concentration due to the temperature fluctuations (Note S.6, ESI†). The vapor mass flux showed an exponential decrease with the stage number (Fig. 3d) due to the sidewall heat loss and the nonlinear relationship between temperature and vapor concentration. The first several stages contributed the most to the total efficiency – with the first three stages accounting for 45% of the total vapor flux. This result shows the importance of optimizing the number of stages since the marginal benefit of adding more stages monotonically decreases while the material cost of each stage remains constant.

To show the significance of vaporization enthalpy recycling, we compared the performance of the ten-stage device with a single-stage device. The demonstrated solar-to-vapor conversion efficiency of the one-stage device with thermal insulation was only 81% (Fig. 3e) which agreed well with the theoretically predicted efficiency (83%). The corresponding water production rate was 1.21 L m^{-2} h^{-1}, which is about five-time smaller than the performance of the ten-stage design (Fig. 3c). For this one-stage device, conduction across the air gap and convection and radiation at the front were dominant sources of loss. Heat loss from the sidewall was negligible for one-stage device due to the small sidewall area. To elucidate the importance of thermal design, we compared the performance of a thermally insulated ten-stage device with a ten-stage device without sidewall insulation. The solar-to-vapor conversion efficiency of the non-insulated ten-stage device degraded to only 286% if the sidewall thermal insulation was removed, where the corresponding predicted efficiency was 326% (Fig. 3e).

Fig. 4 shows a comparison of the demonstrated solar-to-vapor conversion efficiency of our TMSS prototype with several recent works on passive solar vapor generation and desalination. We achieved a record-high solar-to-vapor conversion efficiency

using this ten-stage TMSS device with optimized heat and mass transport performance. The solar-to-vapor conversion efficiency achieved by most past works was below 100% as the thermal energy released from condensation was not reused. Some very recent works which utilized vaporization enthalpy recycling achieved better performance. Li et al. demonstrated 72.2% solar-to-vapor conversion efficiency in conjunction with 1.23% electricity conversion efficiency under 30-sun illumination.[25] Chiavazzo et al. presented the first experimental demonstration to surpass 100% efficiency using vaporization enthalpy recycling.[32] They achieved 218% energy efficiency on a membrane-based ten-stage device using electrical heating, while the efficiency decreased to 138% when the device was powered by solar illumination.[32] Wang et al. used similarly membrane distillation with enthalpy recycling, and 195% solar-to-vapor conversion efficiency was achieved.[33] In comparison, this work nearly doubled the best reported performance using unconcentrated sunlight as the input with advanced heat and mass transfer design.

We also studied the desalination performance of the TMSS prototype using simulated seawater with 3.5 wt% NaCl. After desalination, the salinity of the water (0.0005 wt%) was reduced by four orders of magnitude (Fig. 5a), which is significantly lower than the global drinking water standard set by the World Health Organization (0.02 wt%, WHO).[44] As the salt-accumulation is one of the major barriers for continuous operation,[8,45–47] we tested the salt-rejection performance of the TMSS prototype. To do so, we exposed the first stage of the TMSS device to 1.5 sun illumination (1500 W m^{-2}) for 3.5 hours to simulate continuous operation over a day. The total solar irradiation is 5.25 kW h m^{-2}, which is larger than the US annual average daily solar irradiation (≈ 4.5 kW h m^{-2}).[48] After the 3.5-hour test, we turned off the solar simulator to emulate night time conditions. These operating conditions with high solar flux (1.5 sun) simulated a severe condition which should accelerate salt accumulation and reduce the total diffusion time. Fig. 5b shows the dynamics of
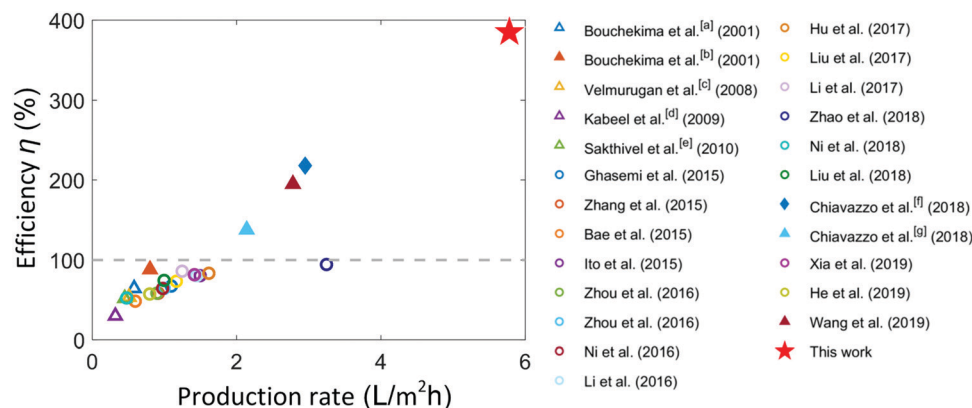

Fig. 4   Comparison of the production rate and solar-to-vapor conversion efficiency with previous reports. Triangles and circles represent solar still experiments (with water collection) and vapor generation experiments (no water collection), respectively. Most of the previous works used interfacial solar heat localization and evaporation on capillary structures.[12,14,15,17–22,24–27,41] The solid markers represent the corresponding studies using multistage configurations.[32,33,42] The diamond marker represents evaporation driven by electrical heating (900 W m^{-2}).[32] The grey-dashed line indicates the efficiency limit (100%) if the vaporization enthalpy is not reused. Most of experiments were performed under one-sun illumination whereas [a], [b], [c] and [g] were under about 600 W m^{-2} solar flux,[10,42] [d] was under 700 W m^{-2} solar illumination,[11] [e] was under 570 W m^{-2} solar illumination,[43] [f] was under 900 W m^{-2} electrical heating.[32]
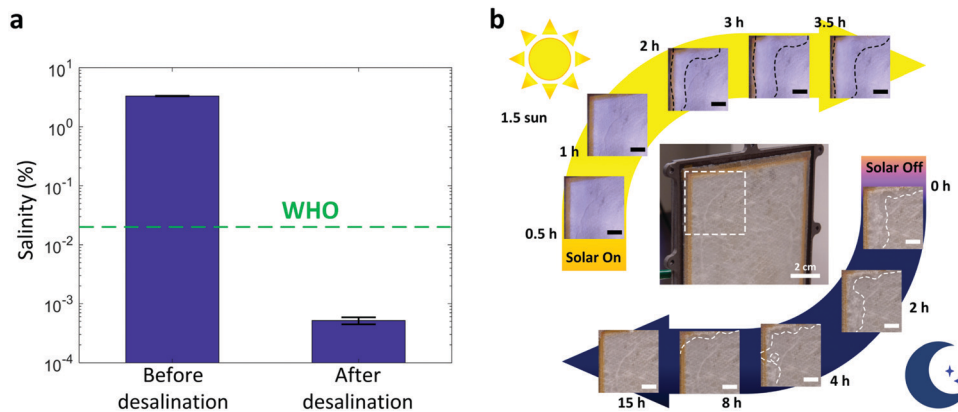
Fig. 5 Solar desalination and salt-rejection performance of the prototype. (a) Salinity of the simulated seawater before and after desalination. The salinity of the water produced by the TMSS prototype was two orders of magnitude lower than the drinking water standard provided by WHO (green-dashed line). (b) Salt-rejection performance during a daytime salt accumulation period and a night time salt diffusion cycle. 1500 W m^{-2} solar illumination was supplied to the TMSS prototype over 3.5 hours to simulate total daily solar irradiation. The largest image at the center shows the evaporator before the experiment started (without salt accumulation). Salt accumulation was observed after two hours on the farthest corners to the reservoir, which had the largest diffusion resistance. After the solar simulator was turned off, the accumulated salt diffused back to the reservoir gradually. The white-dashed box shows the area where most of salt accumulated during the test. The black and white-dashed lines serve as a visual guide and show the approximate area covered by salt and its evolution with time. The scale bars represent one centimeter.

salt accumulation and rejection during an 18.5-hour test. Overall, the evaporator exhibited high salt-rejection capability throughout the test. Salt accumulation was only observed at the two upper corners which had the largest diffusion resistance since they were the farthest distance from the bulk brine. We show detailed evolution of salt accumulation and diffusion at one of these two upper corners (white-dashed box, Fig. 5b). Salt crystals did not appear during the first two hours due to the high solubility of NaCl in water (35.7 mg ml^{-1}) and the relatively high diffusive transport of salt in the evaporator. After two hours, salt began to crystallize and accumulate at the corner. After 3.5-hour operation, the crystallized salt covered approximately 45% of the 4×4 cm^2 area at the corner. The curved black-dashed lines serve as visual guides to show the evolution of salt accumulation. After the solar simulator was turned off, the salt began to diffuse back and the salt accumulation region, depicted by the curved white-dashed lines, depleted. Almost all of the salt on the evaporator diffused back to the bulk brine after 15 hours, indicating adequate salt-rejection performance.

While the laboratory experiment with constant solar flux characterized the performance of our TMSS prototype under a controlled environment, realistic weather conditions outdoor will inevitably impose dynamic effects such as clouds, solar flux and ambient temperature fluctuations on the proposed device. To further understand the device performance under such conditions, we performed an outdoor experiment on a partly sunny day with scattered clouds (July 13, 2019). The experimental setup was placed on a rooftop at MIT campus (Cambridge, MA, USA) where the ten-stage TMSS prototype was fixed on a frame with 30° tilt angle (Fig. 6a and b). Twelve thermocouples were used to characterize the temperature variations of each stage, and a pyranometer (LP-02, Hukseflux) with the same tilt angle was used to measure the incident solar flux on the absorber (Fig. 6a). The condensed water produced by each stage was collected by an

100 ml graduated cylinder where the real-time variation of the water level during the test was recorded by a camera (Fig. 6b). The total mass loss of the water reservoir was measured by a balance. The experiment started at 11:10 am (local time) and ended around 4:00 pm (local time). The temperature of each stage rose up rapidly during the first one hour where the temperature of solar absorber reached more than 30 °C higher than the ambient temperature (Fig. 6c). Water began to flow out from the first stage after 20 minutes (Video S3, ESI†). The solar flux varied significantly from $\approx$200 to 800 W m^{-2} due to the scattered clouds (Fig. 6d and Video S3, ESI†), leading to fluctuations of the solar absorber temperature (Fig. 6c). In particular, each spike in the measured solar flux due to the clouds corresponds to a temperature drop-and-recovery (Fig. 6d). The temperature decreased rapidly with the decrease of solar flux and took a longer time ($\approx$10 minutes) to recover the peak temperature due to thermal inertia (Fig. 6c). Since the weather became cloudier in the afternoon (Fig. 6d), the corresponding solar absorber temperature was more unstable ($\approx$50–65 °C). The temperature fluctuation in each stage led to variation in water collection rate ($\approx$10–20 ml h^{-1}), which was extracted from the water level in the graduated cylinder (Video S3, ESI†). Fig. 6e shows the increase in water level over the collection period. We collected 72 ml of water in total during 4.5 hours, which corresponds to an average productivity of 2.6 L kW^{-1} h^{-1}. Although the cloudy weather and solar flux fluctuation can significantly degrade the overall performance, this ten-stage TMSS prototype still demonstrates a record-high outdoor productivity compared with current state-of-the-art technologies.[27,32] To meet the average daily water intake for one adult ($\approx$3.2 L),[49] 100 TMSS devices can be placed into a 10×10 array, filling an 1 m^2 area, which would provide approximately 10–20 L of clean water every day depending on the weather condition. The upper bound of the water production is according to the performance in laboratory conditions, while the
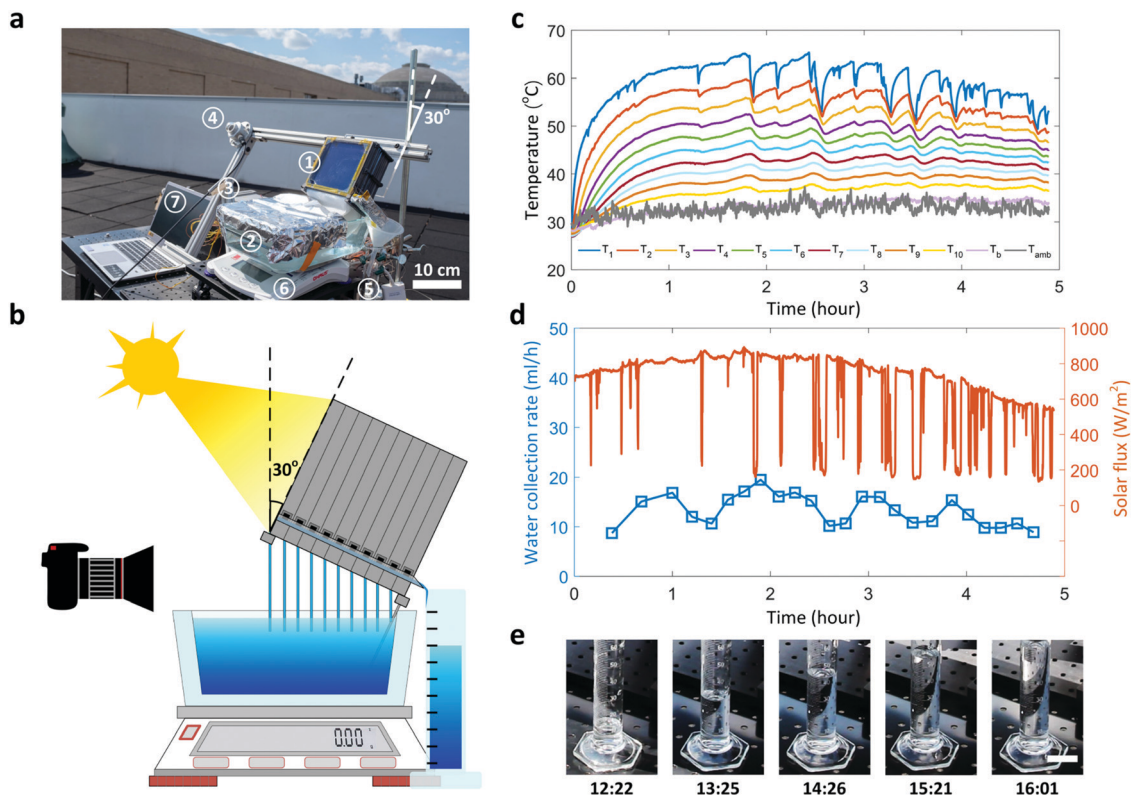
Fig. 6 Outdoor experiments with the ten-stage TMSS prototype on a partly sunny day with scattered clouds on a rooftop at MIT campus (July 13, 2019). (a) Experimental setup. The experimental test rig consisted of (1) a ten-stage TMSS device, (2) a water reservoir, (3) an aluminum extrusion frame, (4) a pyranometer, (5) an 100 ml graduated cylinder, (6) a balance, and (7) a computer. (b) Schematic of the experimental setup. The TMSS device was tilted by 30° to face the sunlight. Condensed water was collected in an 100 ml graduated cylinder where the real-time change of water level was recorded by a camera. (c) Real-time temperature variation of each stage and ambient environment during the outdoor test. (d) Variation in solar flux and water collection rate over time. The significant fluctuation of solar flux due to clouds, led to variation in water collections rate over time. The peak collection rate was 20 ml h^{-1}. (e) Time-lapse images of the collected water in the graduated cylinder. The scale bar represents three centimeters.

lower bound of water production is estimated from the outdoor performance with a partly sunny day.

Conclusions

In summary, we developed a thermally-localized multistage solar still (TMSS) that uses the concept of interfacial solar heat localization and vaporization enthalpy recycling. We show the bottleneck of TMSS performance is the heat and mass transport through the device, which can be significantly improved by optimizing the device geometry (including the evaporator size and the air gap thickness), number of stages, and sidewall thermal insulation. According to the proposed design strategy, a ten-stage TMSS prototype was built based on optimized design parameters using low-cost materials, and then tested under both laboratory and outdoor environments. A record-high solar-to-vapor conversion efficiency of 385% with a water evaporation rate of 5.78 L m^{-2} h^{-1} was demonstrated based on our design. The GOR of this TMSS design was larger than four. The dynamic behavior of heat and mass transport in each stage was characterized experimentally and analyzed theoretically. High desalination and salt-rejection capabilities were also experimentally confirmed using simulated seawater. This work describes the possibility of

achieving high-performance desalination enabled by a system-level heat and mass transport analysis, and demonstrates a practical solution with the TMSS architecture for various off-grid and water-stressed areas.

Author contributions

Z. X., L. Zhang, L. Zhao, and B. L. contributed equally to this work. Z. X., and L. Zhang conceived the initial concept. L. Zhang, Z. X., and L. Zhao developed the theoretical model and optimized the design parameters. Z. X., B. L., L. Zhang, and L. Zhao designed and built the TMSS prototype. L. Zhang, L. Zhao and Z. X. performed the experiments and processed the experimental data. Z. X., L. Zhang, L. Zhao, B. L., and C. W. interpreted the theoretical and experimental results. B. B. performed the UV-vis-NIR characterization. K. L. W. characterized contact angles. Y. S. conducted the SEM characterization. O. L. measured the salinity of the vaporized water. L. Zhang, Z. X., L. Zhao, B. B., B. L., and E. N. W. wrote the paper. J. H. L., R. W., and E. N. W. guided the overall project.

Conflicts of interest

There are no conflicts to declare.

This journal is © The Royal Society of Chemistry 2020

Energy Environ. Sci., 2020, **13**, 830–839 | **837**

Acknowledgements

References

1 M. M. Mekonnen and A. Y. Hoekstra, *Sci. Adv.*, 2016, **2**, e1500323.

2 J. Schewe, J. Heinke, D. Gerten, I. Haddeland, N. W. Arnell, D. B. Clark, R. Dankers, S. Eisner, B. M. Fekete, F. J. Colón-González, S. N. Gosling, H. Kim, X. Liu, Y. Masaki, F. T. Portmann, Y. Satoh, T. Stacke, Q. Tang, Y. Wada, D. Wisser, T. Albrecht, K. Frieler, F. Piontek, L. Warszawski and P. Kabat, *Proc. Natl. Acad. Sci. U. S. A.*, 2014, **111**, 3245–3250.

3 M. Elimelech and W. A. Phillip, *Science*, 2011, **333**, 712–717.

4 A. D. Khawaji, I. K. Kutubkhanah and J.-M. Wie, *Desalination*, 2008, **221**, 47–69.

5 M. Qasim, M. Badrelzaman, N. N. Darwish, N. A. Darwish and N. Hilal, *Desalination*, 2019, **459**, 59–104.

6 R. F. Service, *Science*, 2006, **313**, 1088.

7 S. A. Kalogirou, *Prog. Energy Combust. Sci.*, 2005, **31**, 242–281.

8 G. Ni, S. H. Zandavi, S. M. Javid, S. V. Boriskina, T. A. Cooper and G. Chen, *Energy Environ. Sci.*, 2018, **11**, 1510–1519.

9 F. E. Ahmed, R. Hashaikeh and N. Hilal, *Desalination*, 2019, **453**, 54–76.

10 V. Velmurugan, M. Gopalakrishnan, R. Raghu and K. Srithar, *Energy Convers. Manage.*, 2008, **49**, 2602–2608.

11 A. Kabeel, *Energy*, 2009, **34**, 1504–1509.

12 H. Ghasemi, G. Ni, A. M. Marconnet, J. Loomis, S. Yerci, N. Miljkovic and G. Chen, *Nat. Commun.*, 2014, **5**, 4449.

13 Z. Wang, Y. Liu, P. Tao, Q. Shen, N. Yi, F. Zhang, Q. Liu, C. Song, D. Zhang, W. Shang and T. Deng, *Small*, 2014, **10**, 3234–3239.

14 K. Bae, G. Kang, S. K. Cho, W. Park, K. Kim and W. J. Padilla, *Nat. Commun.*, 2015, **6**, 10103.

15 Y. Ito, Y. Tanabe, J. Han, T. Fujita, K. Tanigaki and M. Chen, *Adv. Mater.*, 2015, **27**, 4302–4307.

16 Y. Liu, S. Yu, R. Feng, A. Bernard, Y. Liu, Y. Zhang, H. Duan, W. Shang, P. Tao, C. Song and T. Deng, *Adv. Mater.*, 2015, **27**, 2768–2774.

17 L. Zhang, B. Tang, J. Wu, R. Li and P. Wang, *Adv. Mater.*, 2015, **27**, 4889–4894.

18 X. Li, W. Xu, M. Tang, L. Zhou, B. Zhu, S. Zhu and J. Zhu, *Proc. Natl. Acad. Sci. U. S. A.*, 2016, **113**, 13953–13958.

19 G. Ni, G. Li, S. V. Boriskina, H. Li, W. Yang, T. Zhang and G. Chen, *Nat. Energy*, 2016, **1**, 16126.

20 L. Zhou, Y. Tan, D. Ji, B. Zhu, P. Zhang, J. Xu, Q. Gan, Z. Yu and J. Zhu, *Sci. Adv.*, 2016, **2**, e1501227.

21 L. Zhou, Y. Tan, J. Wang, W. Xu, Y. Yuan, W. Cai, S. Zhu and J. Zhu, *Nat. Photonics*, 2016, **10**, 393.

22 X. Hu, W. Xu, L. Zhou, Y. Tan, Y. Wang, S. Zhu and J. Zhu, *Adv. Mater.*, 2017, **29**, 1604031.

23 C. Jia, Y. Li, Z. Yang, G. Chen, Y. Yao, F. Jiang, Y. Kuang, G. Pastel, H. Xie, B. Yang, S. Das and L. Hu, *Joule*, 2017, **1**, 588–599.

24 H. Liu, X. Zhang, Z. Hong, Z. Pu, Q. Yao, J. Shi, G. Yang, B. Mi, B. Yang, X. Liu, H. Jiang and X. Hu, *Nano Energy*, 2017, **42**, 115–121.

25 X. Li, X. Min, J. Li, N. Xu, P. Zhu, B. Zhu, S. Zhu and J. Zhu, *Joule*, 2018, **2**, 2477–2484.

26 H. Liu, C. Chen, G. Chen, Y. Kuang, X. Zhao, J. Song, C. Jia, X. Xu, E. Hitz, H. Xie, S. Wang, F. Jiang, T. Li, Y. Li, A. Gong, R. Yang, S. Das and L. Hu, *Adv. Energy Mater.*, 2018, **8**, 1701616.

27 F. Zhao, X. Zhou, Y. Shi, X. Qian, M. Alexander, X. Zhao, S. Mendez, R. Yang, L. Qu and G. Yu, *Nat. Nanotechnol.*, 2018, **13**, 489.

28 P. Tao, G. Ni, C. Song, W. Shang, J. Wu, J. Zhu, G. Chen and T. Deng, *Nat. Energy*, 2018, **3**, 1031–1041.

29 Z. Wang, T. Horseman, A. P. Straub, N. Y. Yip, D. Li, M. Elimelech and S. Lin, *Sci. Adv.*, 2019, **5**, eaax0763.

30 H. Tanaka, T. Nosoko and T. Nagata, *Desalination*, 2000, **130**, 279–293.

31 G. Xue, Q. Chen, S. Lin, J. Duan, P. Yang, K. Liu, J. Li and J. Zhou, *Global Challenges*, 2018, **2**, 1800001.

32 E. Chiavazzo, M. Morciano, F. Viglino, M. Fasano and P. Asinari, *Nat. Sustainability*, 2018, **1**, 763.

33 W. Wang, Y. Shi, C. Zhang, S. Hong, L. Shi, J. Chang, R. Li, Y. Jin, C. Ong, S. Zhuo and P. Wang, *Nat. Commun.*, 2019, **10**, 3012.

34 L. Zhao, B. Bhatia, S. Yang, E. Strobach, L. A. Weinstein, T. A. Cooper, G. Chen and E. N. Wang, *ACS Nano*, 2019, **13**, 7508–7516.

35 E. Strobach, B. Bhatia, S. Yang, L. Zhao and E. N. Wang, *J. Non-Cryst. Solids*, 2017, **462**, 72–77.

36 L. A. Weinstein, K. McEnaney, E. Strobach, S. Yang, B. Bhatia, L. Zhao, Y. Huang, J. Loomis, F. Cao, S. V. Boriskina, Z. Ren, E. N. Wang and G. Chen, *Joule*, 2018, **2**, 962–975.

37 R. S. Hansen, C. S. Narayanan and K. K. Murugavel, *Desalination*, 2015, **358**, 1–8.

38 L. Zhang, Z. Xu, B. Bhatia, B. Li, L. Zhao and E. N. Wang, unpublished work.

39 Z. Xu, L. Zhang, K. Wilke and E. N. Wang, *Langmuir*, 2018, **34**, 9085–9095.

40 L. Zhang, J. Zhu, K. L. Wilke, Z. Xu, L. Zhao, Z. Lu, L. L. Goddard and E. N. Wang, *ACS Nano*, 2019, **13**, 1953–1960.

41 Y. Li, T. Gao, Z. Yang, C. Chen, W. Luo, J. Song, E. Hitz, C. Jia, Y. Zhou, B. Liu, B. Yang and L. Hu, *Adv. Mater.*, 2017, **29**, 1700981.

42 B. Bouchekima, B. Gros, R. Ouahes and M. Diboun, *Desalination*, 2001, **137**, 31–38.

43 M. Sakthivel, S. Shanmugasundaram and T. Alwarsamy, *Desalination*, 2010, **264**, 24–31.

44 Guidelines for drinking-water quality, World Health Organization, 2011.

45 S. He, C. Chen, Y. Kuang, R. Mi, Y. Liu, Y. Pei, W. Kong, W. Gan, H. Xie, E. Hitz, C. Jia, X. Chen, A. Gong, J. Liao, J. Li, Z. J. Ren, B. Yang, S. Das and L. Hu, *Energy Environ. Sci.*, 2019, **12**, 1558–1567.

46 Y. Xia, Q. Hou, H. Jubaer, Y. Li, Y. Kang, S. Yuan, H. Liu, M. W. Woo, L. Zhang, L. Gao, H. Wang and X. Zhang, *Energy Environ. Sci.*, 2019, **12**, 1840–1847.

47 Y. Kuang, C. Chen, S. He, E. M. Hitz, Y. Wang, W. Gan, R. Mi and L. Hu, *Adv. Mater.*, 2019, 1900498.

48 N. R. E. Laboratory, U.S. State Solar Resource Maps, https://www.nrel.gov/gis/solar.html, accessed 19 July, 2019.

49 M. N. Sawka, S. N. Cheuvront and R. Carter, *Nutr. Rev.*, 2005, **63**, S30–S39.

This journal is © The Royal Society of Chemistry 2020

Energy Environ. Sci., 2020, **13**, 830–839 | **839**